https://doi.org/10.5194/egusphere-2026-4215
Preprint. Discussion started: 10 August 2026

Radiative-cooling-induced aerosol activation sustains the fog-top feedback by weakening sedimentation in Yellow Sea advection fog

Peidong Xu[1†], Wei Dai[2†], Ziqi Qiao[3], Chun Li[1], Jing-Wu Liu[1*], Xiaorong Gao[4*]

[1]State Key Laboratory of Physical Oceanography, Ocean University of China, Qingdao, China

[2]Qingdao Eco-environment Monitoring Center of Shandong Province, Qingdao, China

[3]Dalian Meteorology Service Center, Dalian Meteorological Bureau, Dalian, China

[4]Guangzhou Meteorological Observatory, Guangzhou Meteorological Bureau, Guangzhou, China

[†]These authors contributed equally to this work.

[*]Corresponding authors: Jing-Wu Liu, Ocean University of China, 238 Songling Road, Qingdao, 266100, P. R. China

Email: liujingwu@126.com; liujingwu@ouc.edu.cn

Xiaorong Gao, Guangzhou Meteorological Bureau, No. 68 Zhicun Industrial First Road, Guangzhou, 511430, P. R. China

Email: xrgao@gz.gov.cn

https://doi.org/10.5194/egusphere-2026-4215
Preprint. Discussion started: 10 August 2026

Abstract

Advection fog remains difficult to simulate because microphysics, radiation, and turbulence are tightly coupled in the shallow fog layer. At the fog top, longwave cooling promotes condensation and liquid-water accumulation, which further strengthens radiative cooling and forms a positive feedback. Although two-moment schemes predict liquid-water mass and droplet number, aerosol activation is commonly driven by updrafts, whereas fog supersaturation often arises from radiative cooling. How radiative-cooling-induced activation affects droplet sedimentation and this fog-top feedback remains unclear. We incorporate radiative-cooling-induced activation into the Thompson aerosol-aware microphysics scheme in the Weather Research and Forecasting model and simulate a Yellow Sea advection-fog event. We compare the modified scheme with the original Thompson scheme and the one-moment Lin scheme. Lin produces excessive liquid water and an overly deep fog layer, whereas the original Thompson scheme removes liquid water too efficiently and underestimates liquid water path and fog depth. The modified scheme better reproduces visibility and liquid water path, reducing the liquid water path bias to -3.14 g m^{-2} and the root-mean-square error to 20.28 g m^{-2}. Liquid-water budget analyses show that cooling-induced activation increases droplet number and reduces droplet size near the fog top, weakening gravitational sedimentation and sustaining the feedback. Sensitivity experiments confirm that sedimentation constrains this feedback and that its strength depends on background aerosol loading. These results suggest that radiative-cooling-induced activation regulates marine-fog liquid water by weakening size-dependent droplet sedimentation, highlighting the need to represent both processes in two-moment microphysics schemes.

https://doi.org/10.5194/egusphere-2026-4215
Preprint. Discussion started: 10 August 2026

1. Introduction

Sea fog frequently occurs over coastal and offshore waters and is often associated with sharply reduced near-surface visibility (Wang, 1983; Leipper, 1994; Lewis et al., 2004). Such low-visibility conditions can disrupt maritime transportation, increase navigation risks, and cause substantial economic losses in fog-prone regions (Gultepe et al., 2007; Koračin et al., 2014; Koračin and Dorman, 2017). Despite their significant impacts on maritime operations and coastal environments, sea fog forecasts remain highly uncertain in numerical weather prediction (NWP) models, largely because the shallow fog layer involves intricate interactions among boundary-layer turbulence, radiation, and cloud microphysical processes that are challenging to represent.

Advection fog represents a dominant marine fog regime in mid-latitude marginal seas, where pronounced SST gradients and persistent cold ocean surfaces create favorable environments for fog formation (Taylor, 1917; Tokinaga et al., 2009; Koračin et al., 2014; Tokinaga and Xie, 2009). Advection fog frequently forms as warm and moist air flows across a colder sea surface, leading to progressive cooling and saturation in the lower marine boundary layer (Wang, 1983). Near-surface turbulent cooling initially promotes condensation and fog formation (Taylor, 1917; Gao et al., 2007). With increasing liquid-water content and optical thickness, the upper part of the fog layer becomes increasingly coupled to radiative processes. Enhanced longwave emission from the fog top then provides a major source of cooling that regulates fog evolution (Rogers and Koračin, 1992; Koračin et al., 2001; Yang et al., 2018). Radiative cooling near the fog top enhances upper-layer condensation and increases liquid-water content. This additional liquid water further modifies the radiative budget, creating a reinforcing feedback that can promote fog development and prolong its lifetime (Yang et al., 2024). Persistent longwave cooling at the fog top can generate turbulent mixing, which promotes the downward transport of warm and dry air from the free atmosphere into the fog layer (Yamaguchi and Randall, 2008; Yang and Gao, 2020). The mixing of dry free-atmospheric air into the fog layer decreases moisture availability near the surface and causes the cloud base to rise, favoring the transition from fog to low-level stratus (Yang et al., 2021).

As fog evolves from a surface-driven regime to a fog-top-driven regime, the liquid-water profile also changes. In the early stage, liquid water content (LWC) is often concentrated near the surface because condensation is primarily driven by near-surface cooling (Brown and Roach, 1976; Nakanishi, 2000; Wærsted et al., 2017). As fog-top longwave cooling intensifies, condensation is preferentially enhanced in the upper fog layer, resulting in increased liquid-water content and a vertical LWC structure closer to adiabatic

https://doi.org/10.5194/egusphere-2026-4215
Preprint. Discussion started: 10 August 2026

conditions (Cermak and Bendix, 2011). In studies of continental radiation fog, the degree to which the LWC profile approaches this adiabatic structure is commonly quantified as fog adiabaticity (Dione et al., 2023). However, the vertical distribution of liquid water in sea fog has received much less attention, mainly because direct observations over the open ocean remain scarce.

Although previous sea-fog simulations have often produced LWC profiles that increase with height (e.g., Gao et al., 2007; Taylor et al., 2021; Chen et al., 2020; Yang et al., 2021), this behavior may partly arise from the inherent assumptions of one-moment microphysics schemes, which predict cloud-water mass while prescribing cloud droplet number concentration. Because many previous sea-fog modeling studies have relied on such schemes (Zhang et al., 2012; Wang et al., 2014; Yang et al., 2019; Yang and Gao, 2020; Kim et al., 2021, 2026), their simulations of the fog-top feedback do not fully account for the effects of droplet number concentration and size-dependent microphysical processes.

One common limitation of one-moment sea-fog simulations is their tendency to overestimate LWC, producing excessively dense fog (e.g., Chen et al., 2020; Taylor et al., 2021). Because visibility in NWP models is commonly diagnosed from cloud water content (Kunkel, 1984; Gultepe et al., 2006), this liquid-water bias directly leads to underestimated visibility. In such schemes, cloud water is diagnosed through saturation adjustment rather than explicitly predicted, with condensation occurring whenever the thermodynamic state exceeds saturation and the corresponding latent heating being included. This treatment assumes that condensation occurs whenever saturation is reached and does not explicitly represent aerosol activation. Because droplet number concentration is not prognosed in one-moment schemes, variations in droplet size and the associated size-dependent gravitational sedimentation cannot be adequately represented. A more physically consistent treatment of fog droplet formation and sedimentation therefore requires, at minimum, a two-moment microphysics framework that predicts both cloud water mass and droplet number concentration.

Nevertheless, most existing two-moment microphysics schemes were primarily developed for convective clouds rather than for fog, which is better regarded as a shallow stratiform cloud system (e.g., Morrison et al., 2009; Thompson and Eidhammer, 2014). Their direct application to advection fog may therefore inadequately represent key fog microphysical processes. A key issue is the treatment of aerosol activation. In many two-moment schemes, aerosol activation is parameterized mainly in terms of updraft speed, whereas vertical velocities in fog are weak and supersaturation is often generated by diabatic cooling, particularly longwave radiative cooling near the fog top. Recent studies

https://doi.org/10.5194/egusphere-2026-4215
Preprint. Discussion started: 10 August 2026

of continental fog have shown that including radiative cooling in activation calculations can substantially affect simulated droplet number concentrations. For example, Ghosh et al. (2025a) demonstrated that aerosol activation in fog simulations can be strongly influenced by radiative cooling. Peterka et al. (2024) further introduced a cooling-dependent activation approach for fog and showed that it enhanced droplet number concentrations in the upper fog layer and extended fog persistence. However, how radiative-cooling-induced activation modifies droplet sedimentation and the fog-top radiative–microphysical feedback in marine advection fog remains unclear.

In this study, we investigate this knowledge gap using a typical advection-fog event over the Yellow Sea, a marginal sea where frequent sea fog strongly affects maritime activities. We use the Weather Research and Forecasting (WRF) model with the two-moment Thompson aerosol-aware microphysics scheme (Thompson and Eidhammer, 2014), in which aerosol activation is driven primarily by updraft speed. We incorporate radiative-cooling-induced activation into the Thompson scheme and compare the modified scheme with the original Thompson scheme and the one-moment Lin scheme (Lin et al., 1983) to determine how the activation treatment modifies droplet sedimentation and the fog-top feedback. This study therefore provides a process-level interpretation of sea-fog simulation biases and highlights the need for fog-oriented microphysics parameterizations that account for both aerosol activation and sedimentation.

The paper is structured as follows. Section 2 presents the observational datasets, model configuration, and diagnostic approaches. Section 3 provides the synoptic evolution of the fog event. Section 4 examines the simulated fog characteristics and sensitivity experiments, followed by a discussion of the underlying mechanisms. Section 5 concludes with the major findings and their broader implications.

2. Data and methods

2.1 *Data sets*

We use the fifth-generation atmospheric reanalysis product from the European Centre for Medium-Range Weather Forecasts (ERA5; Copernicus Climate Change Service (C3S), 2017), which provides hourly atmospheric fields based on the assimilation of a wide range of observations. In this study, multilevel fields of wind, temperature, relative humidity, and geopotential height at a horizontal resolution of 0.25° × 0.25° are used to characterize the large-scale atmospheric conditions during the sea-fog event. Visibility observations from the Baengnyeongdo AB (BYD) station (171 m a.s.l.) are utilized to assess the WRF model's performance in simulating observed visibility variations.

https://doi.org/10.5194/egusphere-2026-4215
Preprint. Discussion started: 10 August 2026

Himawari-8 imagery is used to identify fog-covered areas and track their horizontal evolution (Bessho et al., 2016). During the daytime, the fog deck is identified from red–green–blue (RGB) composite imagery, in which sea fog appears as a bright and horizontally homogeneous cloud layer over the ocean. Nighttime fog detection is based on the spectral contrast between the 3.9 and 10.4 μm infrared channels, with negative brightness temperature differences indicating foggy conditions (Cermak and Bendix, 2007; Ellrod, 1995; Eyre et al., 1984). LWP retrievals from the Advanced Microwave Scanning Radiometer 2 (AMSR2, Remote Sensing Systems et al., 2024) are used to evaluate the simulated LWP. In addition, profiles of 532 nm total attenuated backscatter from the Cloud–Aerosol Lidar and Infrared Pathfinder Satellite Observation (CALIPSO) are used to access the simulated vertical structure of the fog layer (Minnis et al., 2008; Winker, 2026).

2.2 *Model settings*

The WRF model (version 4.5; Skamarock et al., 2019) is used to simulate the sea-fog event. The simulation adopts a two-layer nested configuration with horizontal resolutions of 30 km for the outer domain (20–50° N, 110–150° E) and 10 km for the inner domain (32–45° N, 115–135° E) (Fig. S1a). All analyses are based on the inner-domain output. The model employs 57 vertical levels, with enhanced resolution in the boundary layer and the lowest model level located approximately 8 m above sea level, following Yang et al. (2019). The atmospheric initial state and lateral forcing are provided by ERA5 reanalysis data. Sea surface temperature is prescribed using the GHRSST analysis product (NASA/JPL, 2015) with a horizontal resolution of 0.01° × 0.01°. The simulations start at 08:00 LST (UTC + 8 h) on 24 March 2021 and extend for 66 h, with the first 8 h discarded as model adjustment time before the analysis period.

The physical parameterizations common to all experiments include the Yonsei University planetary boundary layer scheme (Hong et al., 2006), the Kain–Fritsch cumulus scheme (Kain, 2004), and the RRTM for General circulation models shortwave and longwave radiation schemes (Iacono et al., 2000). Two microphysics schemes are evaluated: the Lin scheme (Lin et al., 1983) and the Thompson aerosol-aware microphysics scheme (Thompson and Eidhammer, 2014).

Unlike the Lin scheme, the Thompson aerosol-aware formulation explicitly predicts droplet number together with condensate mass, allowing size-dependent microphysical processes such as gravitational settling to evolve interactively. In the original Thompson aerosol-aware scheme, aerosol activation is parameterized using lookup tables derived from parcel-model simulations (Eidhammer et al., 2009) based on Köhler activation theory

https://doi.org/10.5194/egusphere-2026-4215
Preprint. Discussion started: 10 August 2026

(Köhler, 1936). The lookup variables include vertical velocity, temperature, water-friendly aerosol number concentration, aerosol characteristic radius, and the hygroscopicity parameter. In this study, the default idealized water-friendly aerosol profile is used. The near-surface aerosol number concentration is initialized at 350 cm^{-3} and decreases with height (Figs. S1a and S1c). The aerosol characteristic radius and hygroscopicity parameter are prescribed as 0.04 μm and 0.8, respectively. Based on these prescribed aerosol properties, temperature, vertical velocity, and water-friendly aerosol number concentration, the activated fraction is obtained from a pre-calculated lookup table (Fig. S2).

Following Ghosh et al. (2025a), we convert radiative cooling into an equivalent vertical velocity in the Thompson aerosol-aware scheme. The equivalent vertical velocity (w_{eq}) used for aerosol activation is defined as

$$w_{eq} = w_{ad} + w_{ra} = -\frac{1}{\Gamma_s}(\frac{dT}{dt})_{ad} - \frac{1}{\Gamma_s}(\frac{dT}{dt})_{ra},$$

where w_{ad} and w_{ra} represent the equivalent vertical-velocity contributions from adiabatic ascent and radiative cooling, respectively. Γ_s is the saturated adiabatic lapse rate. $(\frac{dT}{dt})_{ad}$ and $(\frac{dT}{dt})_{ra}$ are the temperature tendencies associated with the adiabatic and radiative processes, respectively. Under this sign convention, a negative temperature tendency associated with cooling produces a positive equivalent vertical velocity. The resulting w_{eq} is then used as the vertical-velocity input to the activation lookup table.

2.3 *Experimental design*

The Lin experiment serves as a reference because the Lin bulk microphysics scheme has been widely used in simulations of Yellow Sea fog (e.g., Yang et al., 2019; Yang and Gao, 2020; Zhang et al., 2024). Unlike the Thompson aerosol-aware scheme, the Lin scheme is a one-moment bulk microphysics scheme that predicts only the cloud water mixing ratio; it neither explicitly represents aerosol activation nor predicts cloud droplet number concentration. Cloud liquid water is produced primarily through saturation adjustment.

Following the naming convention of Ghosh et al. (2025a), the experiment using the standard Thompson aerosol-aware microphysics scheme is denoted AD because aerosol activation in this scheme is driven primarily by adiabatic ascent. The experiment that additionally accounts for radiative-cooling-induced activation is denoted AD-RA. The main analyses compare the Lin, AD, and AD-RA experiments to assess how the use of one- versus two-moment microphysics and the inclusion of radiative-cooling-induced activation influence sea-fog evolution.

Additional sensitivity experiments are designed to further isolate the effects of cloud-

https://doi.org/10.5194/egusphere-2026-4215
Preprint. Discussion started: 10 August 2026

droplet sedimentation and background aerosol conditions. The AD-noSED and AD-RA-noSED experiments are conducted by disabling droplet sedimentation in the AD and AD-RA experiments, respectively. To evaluate the sensitivity of the modified activation scheme to background aerosol conditions, we conduct an additional experiment, AD-RA-highAERO, using a higher aerosol loading than in AD-RA. The default climatological water-friendly aerosol field provided by WRF has been reported to exceed observed concentrations by approximately one order of magnitude (Weston et al., 2022). We therefore scale the climatological aerosol concentrations uniformly by a factor of 0.1 and use the resulting field in AD-RA-highAERO. Even after this scaling, the aerosol number concentrations within the boundary layer remain approximately twice those in the idealized configuration used in AD-RA (Figs. S1b and S1c). Table 1 provides an overview of the experimental configurations.

Table 1. WRF experiment settings.

Experiments	Model settings
Lin	One-moment Lin bulk microphysics scheme
AD	Thompson aerosol-aware microphysics with standard updraft-driven activation
AD-RA	As AD, but including radiative-cooling-induced activation
AD-noSED	As AD, but with droplet sedimentation disabled
AD-RA-noSED	As AD-RA, but with droplet sedimentation disabled
AD-RA-highAERO	As AD-RA, but using higher background aerosol concentrations

2.4 *Liquid water budget analysis*

To diagnose the processes controlling sea-fog evolution, the LWC tendency is decomposed as

$$\frac{\partial LWC}{\partial t} = \left(\frac{\partial LWC}{\partial t}\right)_{\mathrm{mp}} + \left(\frac{\partial LWC}{\partial t}\right)_{\mathrm{turb}} + \left(\frac{\partial LWC}{\partial t}\right)_{\mathrm{adv}},$$

where three right-hand-side terms describe the LWC tendencies associated with microphysical processes, turbulent mixing, and advection, respectively. To isolate the contributions of individual microphysical processes, the total microphysical tendency is further decomposed as

$$\left(\frac{\partial LWC}{\partial t}\right)_{\mathrm{mp}} = \left(\frac{\partial LWC}{\partial t}\right)_{\mathrm{cond/evap}} + \left(\frac{\partial LWC}{\partial t}\right)_{\mathrm{sed}} + \left(\frac{\partial LWC}{\partial t}\right)_{\mathrm{auto}} + \left(\frac{\partial LWC}{\partial t}\right)_{\mathrm{accr}}.$$

The four right-hand-side terms represent the contributions from condensation/evaporation, cloud-water sedimentation, autoconversion of cloud water to rainwater, and accretion of cloud droplets by raindrops, respectively. The corresponding LWP budget is obtained by vertically integrating each LWC tendency term over the fog layer.

2.5 *Fog adiabaticity*

https://doi.org/10.5194/egusphere-2026-4215
Preprint. Discussion started: 10 August 2026

Under ideal adiabatic conditions, LWC increases approximately linearly with height as saturated air rises and water vapor condenses. However, boundary-layer processes can reduce LWC relative to its adiabatic value, leading to a subadiabatic profile. The equivalent fog adiabaticity (α_{eq}) describes how closely the simulated LWC profile within the fog layer follows an ideal adiabatic distribution.

Following Toledo et al. (2021), α_{eq} can be expressed as

$$\alpha_{eq} = \frac{2(LWP - LWC_0 H)}{\Gamma_{ad} H^2},$$

where LWC_0 is the LWC at the fog base, H is the simulated fog-layer thickness, and Γ_{ad} is the adiabatic LWC gradient. Γ_{ad} is calculated as

$$\Gamma_{ad}(T,P) = \rho_d \left[\frac{(\epsilon + r_s) r_s L_v}{R_d T^2} \Gamma_w - \frac{g r_s P}{(P - e_s) R_d T}\right],$$

where T is surface temperature, P is surface pressure, ρ_d is dry-air density, ϵ is the ratio of the gas constant for dry air to that for water vapor, r_s is the saturation mixing ratio, e_s is the saturation vapor pressure, L_v is the latent heat of vaporization, g is gravitational acceleration, R_d is the gas constant for dry air, and Γ_w is the moist-adiabatic lapse rate. A value of α_{eq} close to 1 indicates that the fog layer approaches an ideal adiabatic structure. Values between 0 and 1 indicate a subadiabatic increase in LWC with height, whereas values greater than 1 indicate that LWC increases with height more rapidly than the adiabatic reference. Negative values indicate a bottom-heavy LWC profile, with LWC decreasing on average with height.

3. Synoptic evolution

We investigate a typical advection-fog event over the Yellow Sea during March 24–27, 2021. At 20:00 LST on March 24, a trough extended over the Yellow Sea at 850 hPa (Fig. S3a), while a relatively weak surface high-pressure system was located over the northern Yellow Sea and the Bohai Sea (Fig. S3e). Under this synoptic pattern, weak large-scale subsidence prevailed over the Yellow Sea (not shown). Weak southwesterly winds advected warm, moist air over the colder waters of the northern Yellow Sea, promoting sea-fog formation (Fig. 1a). Under these conditions, the observed visibility at the BYD station dropped below 1 km between 16:00 and 20:00 LST on March 24 (black line in Fig. 2).

Himawari-8 observations showed that the sea fog expanded over the central and eastern Yellow Sea during the night of March 24 (Figs. 1b and 1c). Consistently, the visibility at the BYD station decreased to approximately 0.4 km (Fig. 2). From March 25 to the early morning of March 26, the ridge at 850 hPa over the Yellow Sea gradually

https://doi.org/10.5194/egusphere-2026-4215
Preprint. Discussion started: 10 August 2026

shifted eastward (Figs. S3b and S3c), accompanied by the eastward movement of a surface high-pressure center located northwest of the basin (Figs. S3e, S3f, and S3g). The weak subsidence associated with the anticyclonic flow, together with widespread relative humidity exceeding 90% over the Yellow Sea, provided favorable conditions for fog persistence and development. As solar radiation strengthened after noon on March 25, the fog weakened and visibility improved slightly (Figs. 1d, 1e, and 2). The fog intensified again during the following night, with visibility falling below 0.1 km by the early morning of March 26 (Figs. 1f and 2). By the afternoon of March 26, stronger solar radiation reduced the fog extent, and visibility increased to approximately 10 km (Figs. 1g and 2).

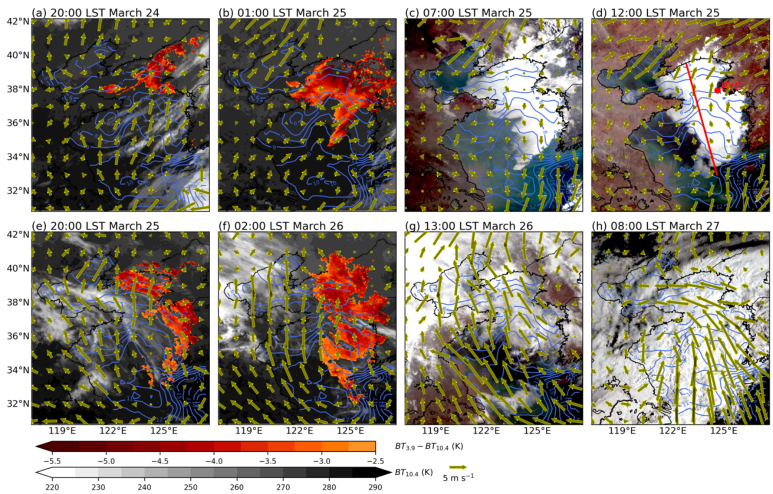

Figure 1. Himawari-8 satellite images superimposed with 10-m winds (vectors in m s^{-1}) and sea surface temperature (blue contours in °C) at (a) 20:00 LST on March 24, (b) 01:00, (c) 07:00, (d) 12:00 and (e) 20:00 LST on March 25, (f) 02:00 and (g) 13:00 LST on March 26, and (h) 08:00 LST on March 27. The daytime panels show visible Red-Green-Blue images. In the nighttime panels, gray shading denotes the 10.4 µm brightness temperature and the red shading denotes the infrared brightness temperature difference between the 3.9 and 10.4 µm channels. The red line and red dot in (d) indicate the CALIPSO overpass track and the Baengnyeongdo AB station, respectively.

By 00:00 LST on March 27, the synoptic circulation over the Yellow Sea had changed markedly. The 850-hPa ridge moved eastward away from the Yellow Sea, while a trough approached the region from the west (Figs. S3d and S3h). The associated large-scale ascent favored the lifting of the sea-fog layer and its transition into low cloud (Fig. 1h). Overall, this case exhibited typical features of advection fog.

4. Simulation results

4.1 *Evaluation of simulated fog against observations*

We first compare the observed and simulated visibility at the BYD station during the fog event (Fig. 2). The Lin experiment produces persistently low visibility, generally below 0.1 km throughout the fog period, indicating excessively dense fog. In contrast, the AD

https://doi.org/10.5194/egusphere-2026-4215
Preprint. Discussion started: 10 August 2026

experiment yields much higher visibility, with intermittent dissipation of the simulated fog. The AD-RA experiment better captures the magnitude and temporal variability of the observed low-visibility conditions.

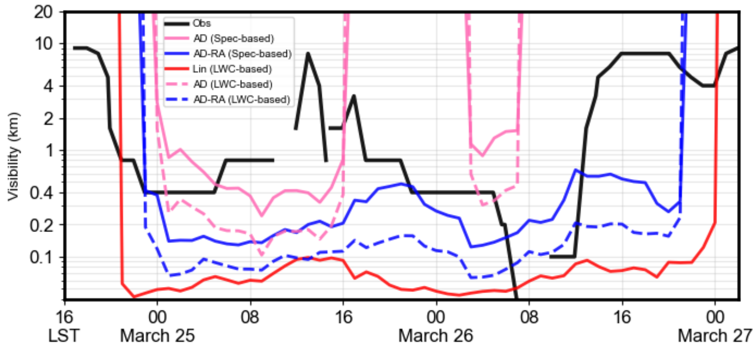

Figure 2. Visibility (km) at the Baengnyeongdo AB station (elevation: 171 m a.s.l.) from observations (black) and the Lin (red), AD (pink), and AD-RA (blue) experiments. Dashed lines show visibility diagnosed using the LWC-based formulation of Kunkel (1984), whereas solid lines show visibility diagnosed using a spectral method based on Mie theory.

The difference between the LWC-based and spectral visibility estimates further indicates that visibility is sensitive not only to LWC but also to the simulated droplet size distribution. This sensitivity is also evident in the horizontal distributions of 10 m visibility (Fig. S4), for which the spectral estimates are generally higher than the LWC-based estimates. However, the low-visibility conditions simulated by the Lin and AD-RA experiments persist for approximately 8–12 h longer than observed. This overestimation of fog duration is associated with a delayed transition from sea fog to low cloud in the simulations (not shown) and may also partly reflect the inadequate representation of daytime heating over the island and the resulting local boundary-layer adjustment. Overall, compared with the Lin and AD experiments, AD-RA provides a more realistic representation of the observed visibility evolution at the elevated island station.

Figure 3 further compares the spatial evolution of LWP in the three simulations with AMSR2 retrievals during the fog event. The AMSR2 retrievals indicate that elevated LWP was concentrated mainly over the central and northern Yellow Sea, with the highest values approaching 100 g m^{-2} near the northeastern portion of the fog deck (Figs. 3d2, 3d4, and 3d5). Among the three experiments, the Lin experiment produces the largest LWP during most of the event (Figs. 3a1–3a6). In particular, at 01:00 and 07:00 LST on March 25 (Figs. 3a2 and 3a3, respectively) and at 02:00 LST on March 26 (Fig. 3a5), the Lin experiment generates extensive areas with LWP exceeding 150 g m^{-2}, especially over the northeastern Yellow Sea. These values are substantially higher than those retrieved from AMSR2, indicating that the one-moment Lin scheme substantially overestimates liquid-water

https://doi.org/10.5194/egusphere-2026-4215
Preprint. Discussion started: 10 August 2026

loading in the fog layer.

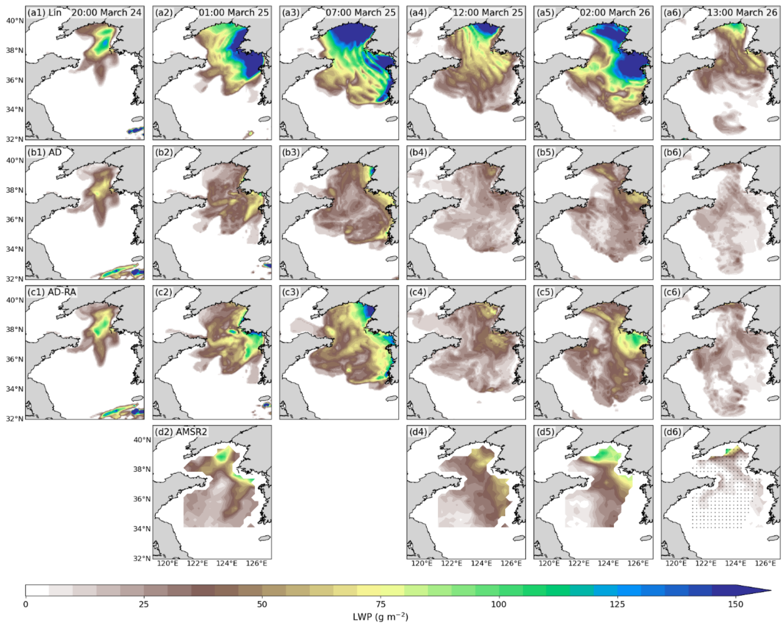

Figure 3. Liquid water path (shaded in g m^{-2}) from the WRF simulations and AMSR2 observations. Rows (a)-(c) show the Lin, AD, and AD-RA experiments, respectively. Row (d) shows AMSR2 retrievals when available. Columns 1–6 correspond to 20:00 LST on March 24, 01:00, 07:00, and 12:00 LST on March 25, and 02:00 and 13:00 LST on March 26, respectively. The dots in (d6) indicate the AMSR2 grid cells that are valid at all four available observation times.

In contrast, the AD experiment markedly reduces LWP across most of the Yellow Sea, yielding values that are generally below the AMSR2 retrievals (Figs. 3b1–3b6). The underestimation is particularly evident over the northern and eastern Yellow Sea. By including radiative-cooling-induced activation, AD-RA produces LWP values that agree more closely with the AMSR2 retrievals (Figs. 3c1–3c6). Compared with AD, AD-RA increases LWP throughout the fog deck while still avoiding the unrealistically high LWP produced by the Lin experiment.

The AMSR2 retrievals show that the area-mean LWP generally ranges from 25 to 35 g m^{-2} during the fog period (Fig. 4). Relative to the AMSR2 retrievals, LWP is generally overestimated in the Lin experiment and underestimated in the AD experiment, whereas AD-RA more closely reproduces the retrieved LWP magnitude. The simulated LWP in all experiments shows a consistent diurnal cycle, characterized by a marked reduction after approximately 08:00 LST on both March 25 and March 26. This decrease is consistent with the enhanced shortwave heating following sunrise.

https://doi.org/10.5194/egusphere-2026-4215
Preprint. Discussion started: 10 August 2026

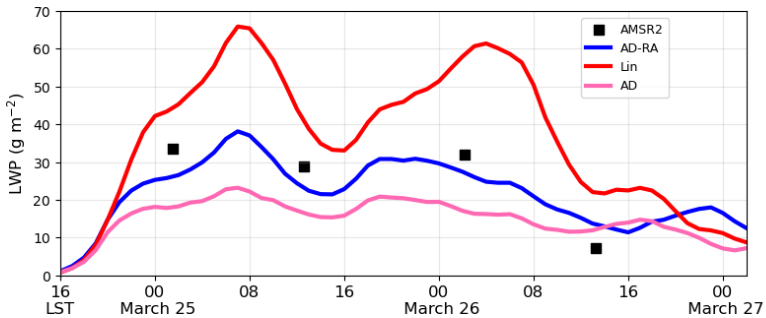

Figure 4. Liquid water path (g m^{-2}) for AMSR2 observations (black squares) and the Lin (red), AD (pink), and AD-RA (blue) experiments. All values are averaged over the common valid AMSR2 grid cells indicated by the dots in Fig. 3d6.

AD-RA improves not only the mean LWP magnitude but also the spatial correspondence of simulated LWP with AMSR2 retrievals within the two-moment framework. In the Lin experiment (Fig. 5a), although the correlation coefficient is relatively high (r = 0.69), the simulated LWP is systematically larger than AMSR2, as indicated by the positive bias of 14.76 g m^{-2} and the largest root-mean-square error (RMSE) of 34.39 g m^{-2}. The AD experiment substantially reduces LWP but shifts the simulation toward underestimation (Fig. 5b), with a lower correlation coefficient (r = 0.47). By including radiative-cooling-induced activation (Fig. 5c), AD-RA achieves the smallest bias (-3.14 g m^{-2}) and the lowest RMSE (20.28 g m^{-2}), while also increasing the correlation coefficient to 0.54 relative to AD.

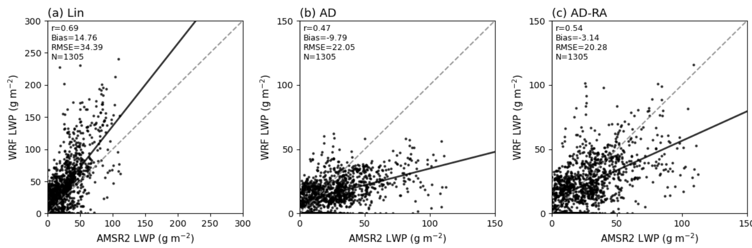

Figure 5. Scatterplots of collocated LWP (g m^{-2}) between AMSR2 observations and WRF simulations from the (a) Lin, (b) AD, and (c) AD-RA experiments. The samples include all valid grid cells from the four available AMSR2 overpasses at 01:00, 12:00 LST on March 25 and 02:00, 13:00 LST on March 26. The dashed gray line indicates perfect agreement between AMSR2 and WRF LWP, and the solid black line represents the linear regression fit. Statistics shown in each panel include the correlation coefficient (r), bias, root-mean-square error (RMSE), and sample size (N). Note that the axis ranges in (a) differ from those in (b) and (c).

Overall, the visibility and LWP comparisons reveal distinct systematic biases among the three experiments. The Lin experiment tends to produce excessive fog liquid water, whereas the AD experiment removes too much liquid water, leading to an underestimation of LWP. In contrast, AD-RA provides a more realistic representation of both visibility and

https://doi.org/10.5194/egusphere-2026-4215
Preprint. Discussion started: 10 August 2026

LWP and therefore yields the best overall agreement with the available observations for this sea-fog event.

4.2 *Vertical structure and fog adiabaticity*

The simulated vertical structures are evaluated against CALIPSO observations along the satellite overpass track at 13:00 LST on March 25 (Fig. 6). CALIPSO indicates a shallow fog layer, with fog-top heights mostly below 150 m and a mean fog-top height of approximately 137.7 m. The Lin experiment produces a much deeper fog layer, with a mean fog-top height of 221.3 m. In contrast, AD produces a slightly shallower fog layer than observed, with a mean fog-top height of 126.9 m. AD-RA deepens the fog layer relative to AD, producing a mean fog-top height of 163.3 m. This response indicates that radiative-cooling-induced activation promotes the vertical development of the fog layer, although the mean fog-top height is somewhat overestimated along this overpass track.

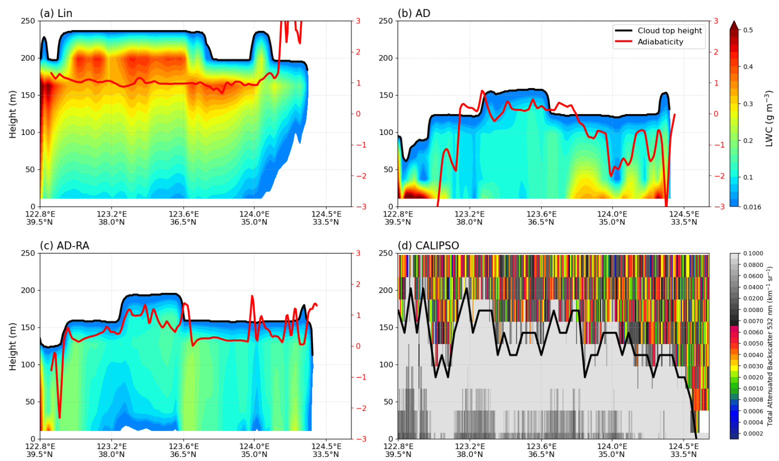

Figure 6. Vertical cross sections along the CALIPSO overpass track at 13:00 LST on March 25. (a)-(c) show simulated liquid water content (shaded in g m^{-3}), simulated cloud-top height (black line in m) and fog adiabaticity (red lines) for the Lin, AD, and AD-RA experiments, respectively. (d) shows the CALIPSO-observed total attenuated backscatter coefficient at 532 nm (shaded in km^{-1} sr^{-1}) together with the retrieved cloud-top height (black line in m). The overpass track is shown by the red line in Fig. 1d.

Adiabaticity quantifies the extent to which the vertical LWC profile within the fog layer approaches its ideal adiabatic form. In the Lin experiment, adiabaticity remains positive and is close to or greater than unity over much of the CALIPSO track, indicating that LWC increases with height at a rate comparable to or greater than the ideal adiabatic rate (Fig. 6a). This vertical structure accompanies the excessive liquid-water accumulation and overly deep fog layer produced by the one-moment scheme. In contrast, the AD experiment shows much lower adiabaticity, with values frequently near zero or negative south of 36° N (Fig. 6b), indicating little vertical increase in LWC or a decrease in LWC with height. Compared with AD, AD-RA produces higher adiabaticity, with values

https://doi.org/10.5194/egusphere-2026-4215
Preprint. Discussion started: 10 August 2026

generally between 0 and 1 along the CALIPSO track (Fig. 6c). These results suggest that the LWC profile in AD is weakly increasing or bottom-heavy, whereas radiative-cooling-induced activation in AD-RA promotes a vertical LWC structure that more closely approaches the ideal adiabatic profile.

We further examine the spatial distribution of adiabaticity at 00:00 LST on March 26 (Fig. 7). Consistent with the cross-section results, the Lin experiment exhibits widespread high adiabaticity over the fog deck, with large areas approaching or exceeding unity (Fig. 7a). This indicates that LWC in the one-moment simulation increases with height at a rate comparable to or greater than the ideal adiabatic rate over much of the fog region. The AD experiment, however, produces much lower adiabaticity, with values near zero or negative over the western part of the fog deck (Fig. 7b), indicating vertically uniform or bottom-heavy LWC profiles. In the AD-RA experiment, the area of negative adiabaticity is smaller and is confined mainly to the western edge of the fog deck, while adiabaticity over the main fog region generally ranges from 0.5 to 1.0 (Fig. 7c). Throughout the fog period, the AD and AD-RA experiments exhibit more pronounced diurnal variations in adiabaticity than the Lin experiment, although the above characteristic differences among the experiments persist throughout the event (Fig. S5).

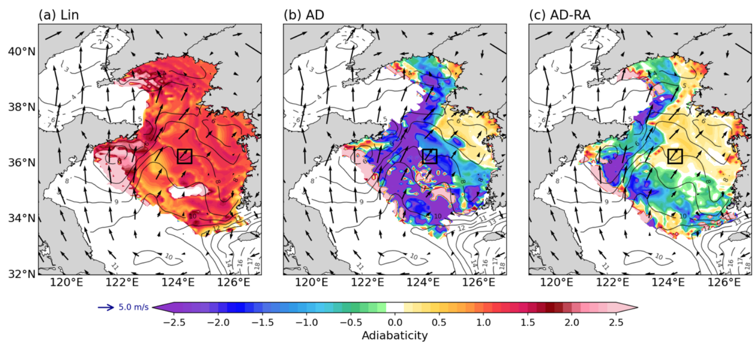

Figure 7. Adiabaticity (shading; dimensionless), 10-m winds (vectors in m s^{-1}) and sea surface temperature (contours in °C) at 00:00 LST on March 26 for the (a) Lin, (b) AD, and (c) AD-RA experiments, respectively. The black rectangles mark the region (124.0–124.5° E, 36.0–36.5° N) selected for the liquid water budget analysis presented in Figs. 9-11 and 13.

To our knowledge, vertically resolved observations of liquid water in sea fog over the open ocean remain scarce, limiting direct evaluation of simulated fog adiabaticity. Nevertheless, observations of continental fog suggest that adiabaticity may increase with LWP, evolving from negative values during the initial stage to approximately 0.6 in more mature fog (Toledo et al., 2021). From this perspective, the widespread adiabaticity exceeding unity in the Lin experiment appears unrealistically high relative to the available continental-fog observations, although its evaluation for marine fog remains uncertain

https://doi.org/10.5194/egusphere-2026-4215
Preprint. Discussion started: 10 August 2026

(Figs. 7a and S5a). The AD experiment exhibits a predominantly bottom-heavy liquid-water structure (Figs. 7b and S5b), whereas AD-RA maintains more liquid water aloft and confines negative adiabaticity mainly to the upwind edge of the fog deck (Figs. 7c and S5c). These results suggest that radiative-cooling-induced activation helps strengthen and sustain the positive feedback in which fog-top longwave cooling promotes liquid-water accumulation, which in turn enhances radiative cooling. This feedback favors a vertical LWC profile that more closely approaches the ideal adiabatic structure.

Figure 8 provides a statistical view of the relationship between fog adiabaticity and LWP across the three experiments. In the Lin experiment, adiabaticity increases rapidly with LWP and approaches unity at LWP values of approximately 40–50 g m^{-2} (Fig. 8a). At higher LWP, the median adiabaticity remains slightly above 1. According to the conceptual framework of Toledo et al. (2021), a fog layer approaching an adiabatic structure exhibits a vertically increasing LWC profile supported by the interaction between fog-top radiative cooling and turbulent mixing. The predominantly positive adiabaticity in the Lin experiment therefore indicates that LWC generally increases toward the fog top. At high LWP, adiabaticity exceeding unity further indicates that this vertical increase is stronger than predicted for an ideal adiabatic profile. This overly strong upper-level liquid-water accumulation accompanies the excessive LWP produced by the one-moment Lin scheme (Fig. 5a).

In contrast, the AD and AD-RA experiments exhibit substantially lower adiabaticity than the Lin experiment. In AD, adiabaticity remains negative over a wide range of LWP and only approaches zero at higher LWP values (Fig. 8b), indicating that LWC generally decreases with height or exhibits little vertical increase in the original Thompson scheme. Including radiative-cooling-induced activation in AD-RA shifts adiabaticity toward more positive values across nearly the entire LWP range (Fig. 8c). Although adiabaticity remains lower than in the Lin experiment, the LWC profile in AD-RA more closely approaches an adiabatic structure than that in AD. This result suggests that radiative-cooling-induced activation near the fog top promotes the formation and retention of liquid water in the upper fog layer, thereby strengthening the positive feedback between fog-top radiative cooling and liquid-water accumulation and allowing the vertical LWC profile to evolve toward a more adiabatic structure.

https://doi.org/10.5194/egusphere-2026-4215
Preprint. Discussion started: 10 August 2026

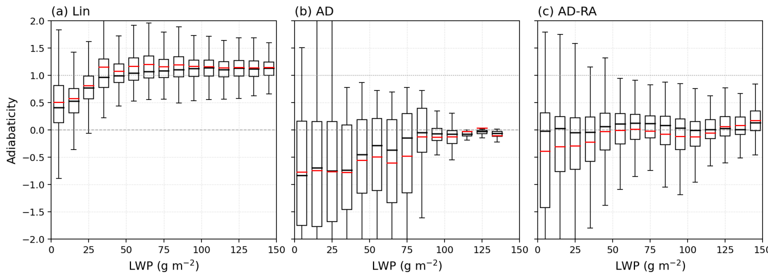

Figure 8. Boxplots of the adiabaticity for different LWP ranges for the (a) Lin, (b) AD, and (c) AD-RA experiments during 16:00 LST March 24 to 00:00 LST March 27. Samples are taken from oceanic grid points within the 121-127° E, 33-40° N region and are grouped into 10 g m^{-2} LWP bins. Only samples for which the lowest-level LWC exceeds 0.016 g m^{-3} are included. Each box denotes the 25th and 75th percentiles, with the black line indicating the median and the red line indicating the mean. The whiskers extend to the minimum and maximum values within 1.5 times the interquartile range. The dashed and dotted horizontal lines indicate adiabaticity values of 0 and 1, respectively.

4.3 *Liquid-water budget analysis*

We use the liquid-water budget to examine how radiative-cooling-induced activation influences the fog-top positive feedback. Figure 9 compares the time–height evolution of the LWC budget terms in the three experiments within the black-outlined region in Fig. 7, where the contrast in adiabaticity between AD and AD-RA remains particularly pronounced during the fog event (Fig. S5). In the Lin experiment, the microphysical tendency (Fig. 9a3) is nearly identical to the condensation/evaporation term (Fig. 9a4), indicating that the cloud-water budget in the one-moment scheme is dominated by saturation adjustment, while the other microphysical processes make little net contribution to the LWC tendency. The condensation/evaporation term shows a pronounced positive contribution aloft and a negative contribution near the fog base. The turbulent tendency exhibits the opposite vertical structure (Fig. 9a2), consistent with the downward redistribution of liquid water by turbulent mixing and the partial offsetting of upper-level liquid-water production associated with fog-top condensation. Nevertheless, adiabaticity remains close to or above unity during most of this period (the red line in Fig. 9a1).

The AD experiment shows a budget structure that differs substantially from that of Lin. The condensation/evaporation term is much weaker than in the Lin experiment and no longer exhibits a pronounced evaporation signal near the fog base (Fig. 9b4). During the early stage of fog development, positive condensation is still present in the upper part of the fog layer. After approximately 19:00 LST on March 25, however, the region of positive condensation moves downward into the lower fog layer (Fig. 9b4), consistent with a substantial weakening of longwave-cooling-driven condensation near the fog top. This weakening is closely associated with the size-dependent representation of droplet sedimentation in the Thompson scheme. Sedimentation transports liquid water from the

https://doi.org/10.5194/egusphere-2026-4215
Preprint. Discussion started: 10 August 2026

upper fog layer toward lower levels (Fig. 9b5), thereby reducing liquid-water accumulation aloft and weakening the positive feedback between fog-top longwave cooling and condensation. Consequently, the LWC profile becomes increasingly bottom-heavy, and negative adiabaticity persists during the fog maintenance stage (Fig. 9b1).

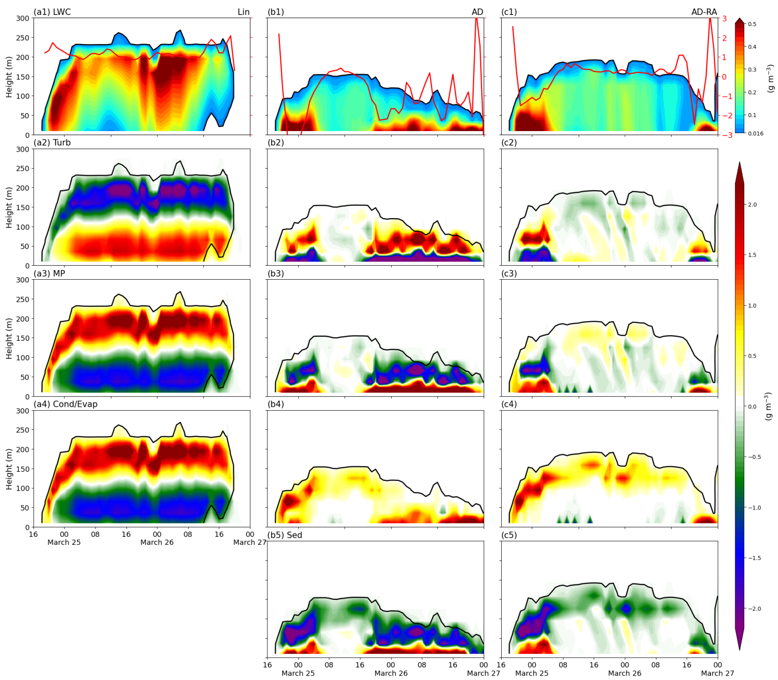

Figure 9. Area-averaged time-height distributions of the LWC budget terms over the region marked by the black rectangles in Fig. 7. Columns (a), (b), and (c) correspond to the Lin, AD, and AD-RA experiments, respectively. Within each column, rows 1-5 show the total LWC change and the contributions from turbulence, microphysics, condensation/evaporation, and sedimentation. Black contours denote the LWC threshold of 0.016 g m^{-3}. (b5) and (c5) show the sedimentation contribution because it is the dominant component among sedimentation, autoconversion, and accretion in the AD and AD-RA experiments.

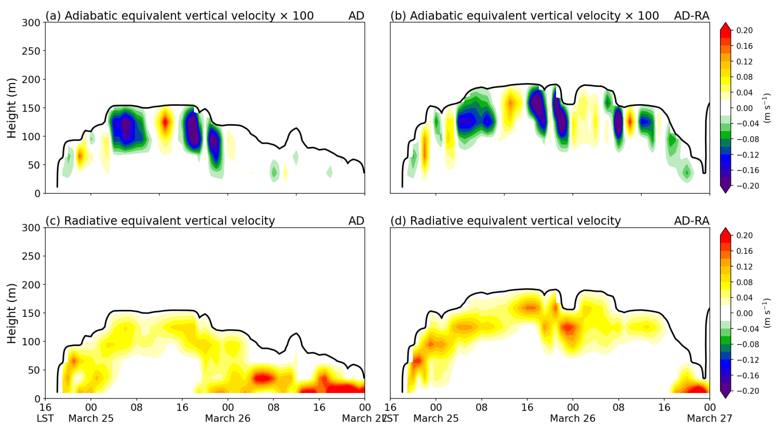

Figure 10. Area-averaged time-height distributions of (a, b) adiabatic equivalent vertical velocity (shaded in m s^{-1}) multiplied by 100, and (c, d) radiative equivalent vertical velocity (shaded in m s^{-1}) over the region

https://doi.org/10.5194/egusphere-2026-4215
Preprint. Discussion started: 10 August 2026

marked by the black rectangles in Fig. 7. The left and right columns correspond to the AD and AD-RA experiments. Black contours denote the LWC threshold of 0.016 g m^{-3}. An equivalent vertical velocity magnitude of 0.15 m s^{-1} corresponds to a temperature change rate magnitude of approximately 0.05 K min^{-1}.

The AD-RA experiment reveals how radiative-cooling-induced activation strengthens the fog-top positive feedback. Compared with AD, the condensation/evaporation tendency is stronger and its positive contribution persists more continuously throughout the upper part of the fog layer in AD-RA (Fig. 9c4), consistent with enhanced condensation where longwave radiative cooling is strongest (Fig. 10d). Although sedimentation continues to produce a negative LWC tendency within the fog layer (Fig. 9c5), its magnitude is smaller than that in AD (Fig. 9b5). This reduction is associated with stronger aerosol activation near the fog top, which increases droplet number concentration (Figs. 11a and 11b), reduces droplet size (Figs. 11c and 11d), and thereby slows gravitational settling and weakens sedimentation. Consequently, the total microphysical tendency in the upper fog layer is less negative in AD-RA than in AD, allowing more liquid water to remain aloft and producing an LWC profile that more closely approaches an adiabatic structure (Figs. 9b1 and 9c1). Together, these results show that radiative-cooling-induced activation sustains upper-level liquid-water accumulation by weakening sedimentation, thereby reinforcing the positive feedback between fog-top longwave cooling and condensation.

The near-base maximum in activated droplet concentration in AD is closely related to the activation treatment in the original Thompson aerosol-aware scheme. Although pronounced longwave radiative cooling develops near the fog top in AD before 18:00 LST on March 25 (Fig. 10c), the original scheme does not explicitly account for this diabatic cooling in its aerosol activation calculation (Fig. 11a). As a result, fewer droplets are activated in the upper fog layer, and the condensed liquid water is distributed among fewer droplets, resulting in larger droplet sizes (Fig. 11c) and stronger gravitational sedimentation (Fig. 9b5). This process suppresses fog-top liquid-water accumulation and coincides with the transition of the LWC profile from a more adiabatic structure to a bottom-heavy structure at approximately 18:00 LST on March 25 (Fig. 9b1).

In contrast to AD-RA, AD also exhibits stronger activation near the fog base. The bottom-heavy liquid-water distribution in AD is accompanied by pronounced longwave radiative cooling in the lower fog layer (Fig. 10c), which can generate local supersaturation (not shown). Once the conditions for activation are met, the original Thompson scheme applies a minimum vertical velocity of 0.01 m s^{-1} in the aerosol activation calculation (Eidhammer et al., 2009). Together with the continuous supply of sea-salt aerosols to the lowest model layer, this minimum-velocity treatment promotes substantial near-base activation and produces a pronounced lower-level maximum in activated droplet

https://doi.org/10.5194/egusphere-2026-4215
Preprint. Discussion started: 10 August 2026

concentration (Fig. 11a).

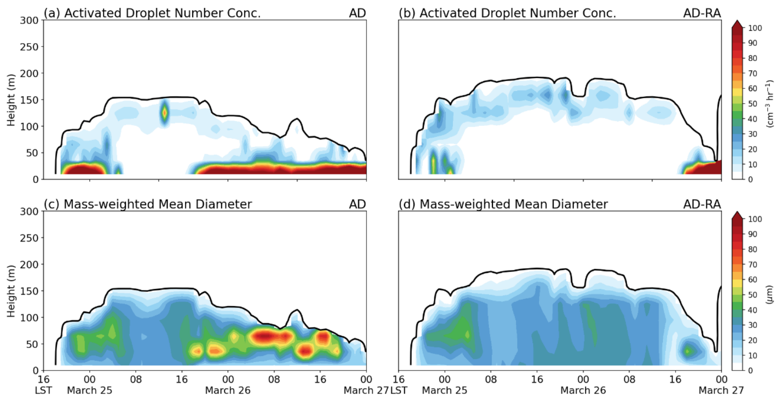

Figure 11. Area-averaged time-height distributions of (a, b) activated-droplet number tendency (shaded in cm^{-3} hr^{-1}) and (c, d) mass-weighted mean diameter (shaded in μm) over the region marked by the black rectangles in Fig. 7. The left and right columns correspond to the AD and AD-RA experiments. Black contours denote the LWC threshold of 0.016 g m^{-3}.

To further test whether the mechanism identified above also operates in more mature fog, we apply the same LWC budget analysis to the central portion of the fog deck (Fig. S5), which is characterized by higher LWP during much of the event (Fig. 3). Although the AD experiment maintains a fog-top positive feedback between longwave radiative cooling and liquid-water accumulation in this region (Figs. S7b1–b4 and S8c), distinct local maxima in longwave radiative cooling develop near both the fog top and fog base after 18:00 LST on March 25 (Fig. S8c). This dipole structure is accompanied by a persistent, gradual lowering of the fog top. In AD-RA, by contrast, radiative-cooling-induced activation helps sustain liquid-water accumulation aloft and keeps the fog-top height at approximately 250 m (Figs. S7c1–c4). This comparison further supports the conclusion that radiative-cooling-induced activation strengthens and sustains the fog-top positive feedback by increasing droplet number concentration near the fog top, maintaining smaller droplets, and limiting the sedimentation-driven depletion of upper-level liquid water.

Figure 12 further presents the cumulative LWP budget for the AD-RA experiment from 08:00 LST on March 24 to 07:00 LST on March 25. The spatial pattern of the simulated net LWP change agrees broadly with that reconstructed from the turbulence, advection, and microphysical contributions (Figs. 12d and 12h), indicating that the diagnosed budget terms capture the main processes responsible for the simulated LWP change. Among these budget components, the microphysical contribution dominates the cumulative LWP change (Fig. 12c), whereas turbulence and advection make smaller and more spatially localized contributions (Figs. 12a and 12b). The decomposition of the microphysical term shows that condensation/evaporation provides the primary positive

https://doi.org/10.5194/egusphere-2026-4215
Preprint. Discussion started: 10 August 2026

contribution to LWP over the fog deck (Fig. 12e), while sedimentation acts as the dominant microphysical sink (Fig. 12g). Autoconversion makes a substantially smaller contribution than either of these processes (Fig. 12f). Therefore, the simulated LWP increase in AD-RA primarily reflects strong condensation that is partly offset by sedimentation loss, with smaller contributions from the other diagnosed processes.

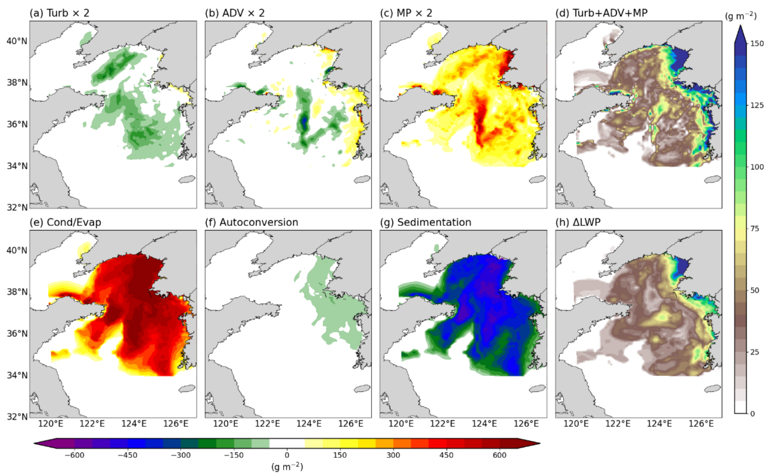

Figure 12. Contributions to the change in liquid water path (h, shaded in g m^{-2}) from 08:00 LST on March 24 to 07:00 LST on March 25 in AD-RA experiment. (a)–(c) show the contributions from turbulence, advection, and microphysics, respectively, with their values multiplied by 2. (d) shows the combined contribution of these three processes. (e)–(g) show the microphysical contributions from condensation/evaporation, autoconversion, and sedimentation, respectively.

Overall, the liquid-water budget analysis shows that radiative-cooling-induced activation affects fog evolution primarily by modifying droplet sedimentation. In AD, weak activation near the fog top results in fewer and larger droplets, leading to stronger sedimentation that limits upper-level liquid-water accumulation and weakens the fog-top positive feedback. In AD-RA, radiative-cooling-induced activation increases droplet number concentration, reduces droplet size, and consequently weakens gravitational settling. This process helps sustain fog-top liquid-water accumulation and the associated radiative feedback, resulting in an LWP evolution that agrees more closely with the observations.

4.4 *Sensitivity to droplet sedimentation and aerosol loading*

To further isolate the role of droplet sedimentation in regulating fog evolution, the AD-noSED experiment disables droplet sedimentation while retaining the standard activation treatment used in AD. Compared with AD (Fig. 9b), AD-noSED produces markedly higher LWC in the upper part of the fog layer and a deeper fog layer (Fig. 13a1). Correspondingly, adiabaticity shifts toward predominantly positive values during much of the fog period. The enhanced upper-level liquid water is accompanied by stronger

https://doi.org/10.5194/egusphere-2026-4215
Preprint. Discussion started: 10 August 2026

condensation near the fog top (Fig. 13a4), consistent with a strengthened positive feedback between liquid-water accumulation and longwave radiative cooling.

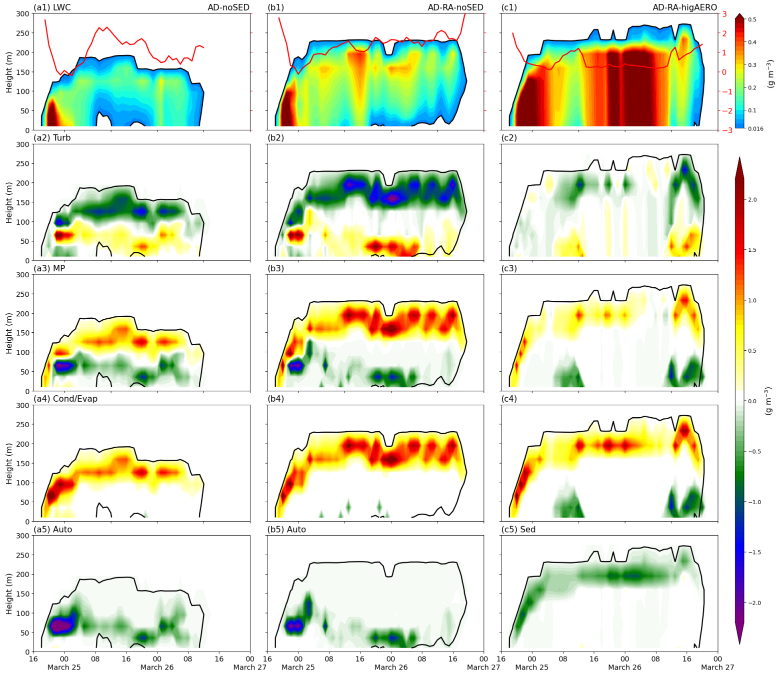

Figure 13. Same as Fig. 9, but for the AD-noSED (a1-a5), AD-RA-noSED (b1-b5) and AD-RA-higAERO (c1-c5) experiments. (a5), (b5), and (c5) show the dominant contribution among sedimentation, autoconversion, and accretion for the corresponding experiments. Specifically, (a5) and (b5) show autoconversion because sedimentation is disabled and accretion is zero in AD-noSED and AD-RA-noSED, whereas (c5) shows sedimentation because it is the dominant liquid-water sink in AD-RA-highAERO.

Although disabling sedimentation substantially reduces the negative microphysical tendency present in AD (Fig. 13a3), this reduction is partly offset by stronger autoconversion (Fig. 13a5), which acts as an alternative sink of cloud liquid water. Nevertheless, the net microphysical depletion of cloud liquid water is greatly reduced. As a result, liquid water produced near the fog top is retained aloft rather than being efficiently transported downward, thereby strengthening the positive feedback between fog-top liquid-water accumulation and longwave radiative cooling. Consistently, visibility in AD-noSED is substantially lower than that in AD throughout the fog period (Fig. 14).

The AD-RA-noSED experiment further shows that removing sedimentation substantially strengthens the fog-top positive feedback relative to AD-RA. AD-RA-noSED produces a deeper fog layer and stronger liquid-water accumulation near the fog top (Fig. 13b1). The corresponding adiabaticity exceeds 1.5, indicating that LWC increases with height much more rapidly than in the ideal adiabatic profile. In this respect, AD-RA-noSED resembles the Lin experiment: adiabaticity remains positive across most of the fog deck

https://doi.org/10.5194/egusphere-2026-4215
Preprint. Discussion started: 10 August 2026

throughout the fog period (Figs. S10b and S11b), accompanied by excessive liquid-water accumulation and a strongly top-heavy LWC structure. The resulting visibility is comparable to the low visibility simulated by Lin and is substantially underestimated relative to the observations (Fig. 14). Moreover, because disabling sedimentation removes an essential fog-layer cloud-water sink, the LWP distribution in AD-RA-noSED departs markedly from the AMSR2 retrievals (Figs. S12b and 3d). These results demonstrate that sedimentation constrains the strength of the fog-top positive feedback and prevents excessive upper-level liquid-water accumulation.

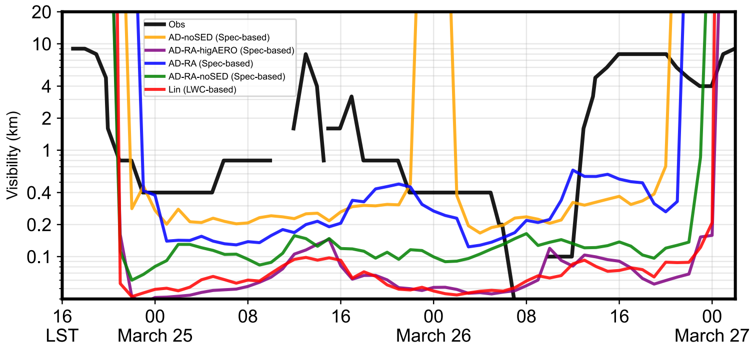

Figure 14. Visibility (km) at the Baengnyeongdo AB station (elevation: 171 m a.s.l.) from observations (black) and the Lin (red), AD-RA (blue), AD-noSED (orange), AD-RA-noSED (green), and AD-RA-highAERO (purple) experiments. Visibility from the Lin experiment is diagnosed using the LWC-based formulation of Kunkel (1984), whereas visibility from the remaining model experiments is diagnosed using a spectral method based on Mie theory.

The AD-RA-highAERO experiment shows that the response to radiative-cooling-induced activation depends strongly on background aerosol loading. Under higher-aerosol conditions, enhanced activation produces a larger cloud droplet number concentration and smaller droplets, thereby weakening gravitational sedimentation. As a result, liquid water produced by condensation in the upper fog layer is less efficiently transported toward lower levels. Compared with AD-RA, AD-RA-highAERO therefore develops a deeper and more persistent fog layer, with higher LWC throughout most of the fog depth (Fig. 13c1). The LWC budget supports this mechanism: condensation remains strong in the upper fog layer (Fig. 13c4), while the negative sedimentation tendency is weaker than that in AD-RA (Fig. 13c5). Thus, condensational liquid-water production aloft is less effectively offset by sedimentation, allowing liquid water to accumulate and persist near the fog top.

Overall, these sensitivity experiments demonstrate that droplet sedimentation provides an essential physical constraint on the fog-top radiative–microphysical feedback in the simulations. Disabling sedimentation in AD-noSED and AD-RA-noSED markedly increases fog adiabaticity, upper-level liquid-water accumulation, and fog-layer depth. The

https://doi.org/10.5194/egusphere-2026-4215
Preprint. Discussion started: 10 August 2026

AD-RA-highAERO experiment further reveals that the effectiveness of radiative-cooling-induced activation is sensitive to the aerosol environment, because changes in aerosol abundance modify droplet number concentrations and associated sedimentation rates. Accurately representing both background aerosol conditions and size-dependent droplet sedimentation is therefore necessary to constrain the fog-top feedback in two-moment sea-fog simulations.

5. Conclusion and discussion

This study investigates how radiative-cooling-induced aerosol activation affects Yellow Sea advection fog within a two-moment microphysics framework. We incorporated the contribution of radiative cooling into the aerosol activation treatment of the Thompson aerosol-aware scheme in WRF. The results show that this additional activation pathway increases droplet number concentration near the fog top, reduces droplet size, and weakens gravitational sedimentation. By retaining more liquid water aloft, radiative-cooling-induced activation sustains the positive feedback between fog-top longwave cooling and liquid-water accumulation, thereby regulating the evolution of the simulated fog.

For the March 24–27, 2021 advection-fog event, the three main experiments exhibit distinct systematic biases. The one-moment Lin scheme produces excessive fog liquid water, resulting in an overly deep fog layer and unrealistically low visibility (Figs. 2, 4, and 6a). In contrast, the original Thompson scheme (AD) produces too little liquid water, underestimates LWP, and yields excessively high visibility with intermittent fog dissipation (Figs. 2, 4, and 6b). Including radiative-cooling-induced activation in AD-RA substantially improves the overall agreement with the available LWP and visibility observations (Figs. 2, 3, and 5c). These contrasts demonstrate that a two-moment framework alone is insufficient for sea-fog simulation when aerosol activation is driven primarily by updraft velocity.

The fog-adiabaticity analysis links the contrasting simulations directly to differences in the vertical distribution of liquid water (Figs. 7, 8, and S5). In Lin, adiabaticity approaches or exceeds unity when LWP reaches approximately 40–50 g m^{-2}, indicating that LWC increases with height at a rate comparable to or greater than that of an ideal adiabatic profile (Fig. 8a). By contrast, adiabaticity in AD is frequently near zero or negative, reflecting a weakly increasing or bottom-heavy LWC profile (Fig. 8b). Radiative-cooling-induced activation in AD-RA shifts adiabaticity toward more positive values, generally between 0 and 1, and produces an LWC profile that more closely approaches an adiabatic structure (Fig. 8c). These differences show that the added activation pathway

https://doi.org/10.5194/egusphere-2026-4215
Preprint. Discussion started: 10 August 2026

supports the retention of liquid water aloft and thereby helps sustain the positive feedback between fog-top longwave cooling and liquid-water accumulation.

The liquid-water budget identifies the processes responsible for these contrasting vertical structures (Fig. 9). In Lin, the total microphysical tendency is nearly identical to the condensation/evaporation tendency, confirming that cloud-water production is dominated by saturation adjustment and that the other microphysical terms provide little compensation (Fig. 9a). Because the one-moment scheme does not represent size-dependent cloud-droplet sedimentation, liquid water produced by fog-top condensation accumulates excessively in the upper fog layer. The resulting increase in liquid water strengthens longwave radiative cooling, while turbulent mixing redistributes part of this water downward. Nevertheless, this turbulent redistribution is insufficient to constrain the fog-top radiative–microphysical feedback, resulting in excessive LWP and an overly deep fog layer.

In AD, the standard updraft-driven activation treatment activates relatively few aerosol particles near the fog top under weak vertical motion (Fig. 11a). Consequently, condensed liquid water is distributed among fewer droplets, producing larger droplets that sediment more rapidly. This enhanced sedimentation transports liquid water out of the upper fog layer, weakens the positive feedback between fog-top longwave cooling and liquid-water accumulation, and results in reduced LWP and limited fog-layer development. In AD-RA, accounting for radiative cooling activates more aerosol particles near the fog top, increases cloud droplet number concentration, and reduces droplet size (Figs. 11b and 11d). The resulting reduction in gravitational sedimentation allows more liquid water to remain aloft (Fig. 9c5), strengthening longwave radiative cooling and the associated condensation. This mutually reinforcing response produces an LWC profile that more closely approaches an adiabatic structure and an LWP that agrees more closely with the AMSR2 retrievals (Figs. 9c1 and 5c). The contrasting mechanisms in AD and AD-RA are summarized schematically in Fig. 15.

The sensitivity experiments further support this mechanism. Disabling droplet sedimentation in AD-noSED markedly increases upper-level liquid water and fog-layer depth (Fig. 13a1). When sedimentation is removed from AD-RA, AD-RA-noSED develops excessive liquid-water accumulation and adiabaticity exceeding 1.5, producing a vertical structure similar to that in Lin (Fig. 13b1). Together, these experiments demonstrate that sedimentation constrains the fog-top radiative–microphysical feedback and is a primary pathway through which radiative-cooling-induced activation affects fog evolution. The AD-RA-highAERO experiment further shows that the magnitude of this response depends

https://doi.org/10.5194/egusphere-2026-4215
Preprint. Discussion started: 10 August 2026

strongly on the prescribed background aerosol loading. Higher aerosol concentrations produce more numerous, smaller droplets, further weaken sedimentation, increase liquid-water accumulation, and reduce visibility (Figs. 13c1 and 14). These results emphasize the need for observation-constrained aerosol fields and surface aerosol sources in two-moment sea-fog simulations.

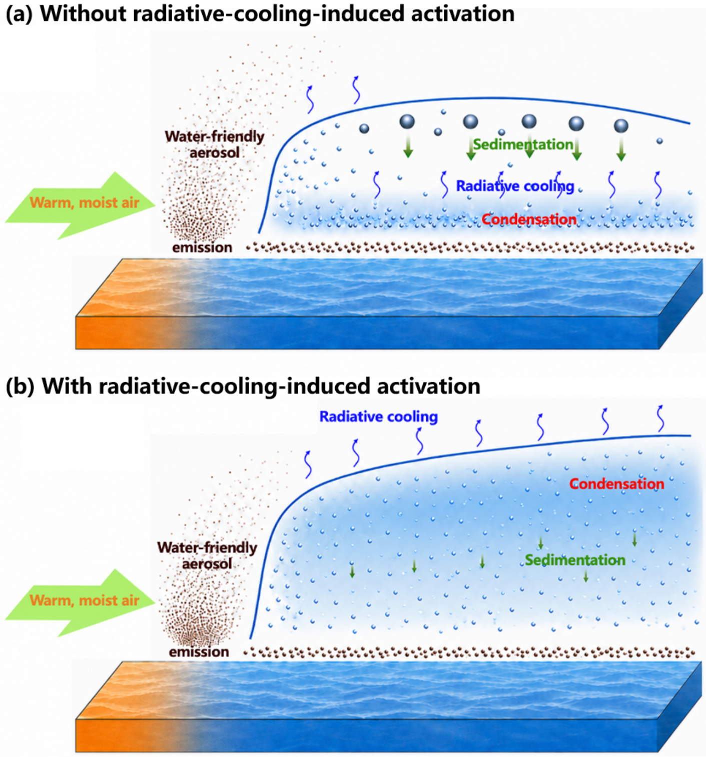

Figure 15. Conceptual diagram summarizing the contrasting mechanisms of sea-fog evolution in the (a) AD and (b) AD-RA experiments. In AD, weak activation of water-friendly aerosols (the brown particles) limits upper-layer condensation, and the produced liquid water (the blue shading) is efficiently removed by sedimentation (the green downward arrows), weakening the fog-top radiative-cooling–condensation feedback and producing a shallower fog layer. In AD-RA, radiative-cooling-induced activation enhances droplet production (the blue droplets) in the upper fog layer. The increased droplet number and reduced droplet size suppress sedimentation, promote liquid-water retention near the fog top, and strengthen the fog-top feedback.

Previous studies have emphasized the importance of fog-water removal in marine-fog simulations. Taylor et al. (2021) showed that insufficient droplet deposition at the sea surface can contribute to overestimated LWC and unrealistically low visibility. Using large-eddy simulations with sectional microphysics, Li et al. (2026) further demonstrated that gravitational droplet sedimentation acts as a vertically coupled process linking fog-top liquid-water production to delayed liquid-water removal near the fog base. The present study extends this view to a mesoscale two-moment microphysics framework by showing

https://doi.org/10.5194/egusphere-2026-4215
Preprint. Discussion started: 10 August 2026

that size-dependent droplet sedimentation constrains the positive feedback between fog-top longwave cooling and liquid-water accumulation. When sedimentation is absent, as in Lin and the no-sedimentation experiments, liquid water accumulates excessively, producing overly large LWP, an excessively deep fog layer, and unrealistically low visibility.

Building on the radiative-cooling-induced activation framework of Ghosh et al. (2025a), the present study demonstrates that the consequences of this activation pathway extend beyond changes in cloud droplet number concentration. In marine advection fog, enhanced activation near the fog top produces more numerous, smaller droplets and thereby weakens size-dependent gravitational sedimentation. The resulting retention of liquid water aloft strengthens the positive feedback between fog-top longwave cooling and condensation. Radiative-cooling-induced activation therefore modifies not only droplet number and size but also the fog-top radiative–microphysical feedback.

Two limitations should be considered when interpreting these results. First, the conclusions are based on a single advection-fog event over the Yellow Sea and therefore cannot establish a general improvement in marine-fog forecast skill. Multi-case simulations and longer-term forecast evaluations across different meteorological regimes are needed to assess the robustness and broader applicability of the modified activation treatment. Second, the experiments primarily use an idealized background distribution and prescribed surface sources of water-friendly aerosols. The AD-RA-highAERO experiment demonstrates that the magnitude of the activation response depends strongly on background aerosol loading. More accurate marine-fog prediction therefore requires both an appropriate representation of radiative-cooling-induced activation and observation-constrained aerosol fields and surface source parameterizations.

Our findings highlight the importance of two-moment microphysics for sea-fog simulation and prediction. Because droplet sedimentation is strongly size dependent, representing this process requires the simultaneous prediction of liquid-water mass and cloud droplet number concentration. However, a two-moment framework alone is insufficient: its performance also depends on a fog-appropriate activation treatment and a realistic representation of the available aerosol population. Previous studies have shown that aerosol activation strongly influences fog droplet number concentration and fog evolution (Ghosh et al., 2025b; Schwenkel and Maronga, 2019), while sea-spray aerosols contribute to marine cloud condensation nuclei (Quinn et al., 2017; Sasakawa and Uematsu, 2002). Together with our aerosol sensitivity results, these findings indicate that reliable sea-fog simulation requires the joint representation of radiative-cooling-induced activation,

https://doi.org/10.5194/egusphere-2026-4215
Preprint. Discussion started: 10 August 2026

size-dependent droplet sedimentation, and observation-constrained aerosol sources.

Code and data availability. The WRF model source code used in this study is publicly accessible through the official WRF repository (https://github.com/wrf-model/WRF). ERA5 reanalysis fields were obtained from the Copernicus Climate Data Store (https://cds.climate.copernicus.eu/). Visibility observations were downloaded from the National Centers for Environmental Information (NCEI; https://www.ncei.noaa.gov/products/land-based-station/integrated-surface-database). CALIPSO data are available from the NASA Langley Atmospheric Science Data Center Distributed Active Archive Center at https://www.earthdata.nasa. gov/data/catalog/larc-cloud-cal-lid-l1-standard-v5-00-v5-00. AMSR2 data are available from Remote Sensing Systems at https://www.remss.com/missions/amsr/. Himawari-8 satellite data are available from the JAXA P-Tree system at https://www.eorc.jaxa.jp/ptree/. GHRSST data are available from the NASA Physical Oceanography Distributed Active Archive Center at https://www.earthdata.nasa.gov/data/catalog/pocloud-mur-jpl-l4-glob-v4.1-4.1. The model output files produced in this study are not publicly archived due to their large size but can be obtained from the corresponding author upon reasonable request.

Author contributions. JWL and WD conceptualized the study and designed the main scientific framework. PDX and ZQ implemented the model modifications and processed the model data. PDX conducted the numerical experiments and analyzed the results, with contributions from WD to the interpretation of the findings. PDX, JWL, and XG prepared the initial draft of the manuscript. CL and WD contributed to the revision and improvement of the manuscript. JWL and XG supervised the research and coordinated the development of the manuscript. All authors participated in the analysis of the results and the revision of the manuscript.

Competing interests. The corresponding author confirms that all authors have no conflicts of interest for this work.

Financial support. This work was supported by the National Natural Science Foundation of China (U2342214 and 42275071).

https://doi.org/10.5194/egusphere-2026-4215
Preprint. Discussion started: 10 August 2026

References

Bessho, K., Date, K., Hayashi, M., Ikeda, A., Imai, T., Inoue, H., Kumagai, Y., Miyakawa, T., Murata, H., Ohno, T., Okuyama, A., Oyama, R., Sasaki, Y., Shimazu, Y., Shimoji, K., Sumida, Y., Suzuki, M., Taniguchi, H., Tsuchiyama, H., Uesawa, D., Yokota, H., and Yoshida, R.: An Introduction to Himawari-8/9— Japan's New-Generation Geostationary Meteorological Satellites, Journal of the Meteorological Society of Japan. Ser. II, 94, 151–183, https://doi.org/10.2151/jmsj.2016-009, 2016.

Brown, R. and Roach, W. T.: The physics of radiation fog: II – a numerical study, Quarterly Journal of the Royal Meteorological Society, 102, 335–354, https://doi.org/10.1002/qj.49710243205, 1976.

Cermak, J. and Bendix, J.: Dynamical Nighttime Fog/Low Stratus Detection Based on Meteosat SEVIRI Data: A Feasibility Study, Pure appl. geophys., 164, 1179–1192, https://doi.org/10.1007/s00024-007-0213-8, 2007.

Cermak, J. and Bendix, J.: Detecting ground fog from space – a microphysics-based approach, International Journal of Remote Sensing, 32, 3345–3371, https://doi.org/10.1080/01431161003747505, 2011.

Chen, C., Zhang, M., Perrie, W., Chang, R., Chen, X., Duplessis, P., and Wheeler, M.: Boundary Layer Parameterizations to Simulate Fog Over Atlantic Canada Waters, 7, https://doi.org/10.1029/2019EA000703, 2020.

Copernicus Climate Change Service (C3S): ERA5: Fifth generation of ECMWF atmospheric reanalyses of the global climate., https://doi.org/https://cds.climate.copernicus.eu/#!/search?text=ERA5&type=dataset, 2017.

Dione, C., Haeffelin, M., Burnet, F., Lac, C., Canut, G., Delanoë, J., Dupont, J.-C., Jorquera, S., Martinet, P., Ribaud, J.-F., and Toledo, F.: Role of thermodynamic and turbulence processes on the fog life cycle during SOFOG3D experiment, Atmospheric Chemistry and Physics, 23, 15711–15731, https://doi.org/10.5194/acp-23-15711-2023, 2023.

Eidhammer, T., DeMott, P. J., and Kreidenweis, S. M.: A comparison of heterogeneous ice nucleation parameterizations using a parcel model framework, Journal of Geophysical Research: Atmospheres, 114, https://doi.org/10.1029/2008JD011095, 2009.

Ellrod, G. P.: Advances in the Detection and Analysis of Fog at Night Using GOES Multispectral Infrared Imagery, Weather and Forecasting, 10, 606–619, https://doi.org/10.1175/1520-0434(1995)010%3C0606:AITDAA%3E2.0.CO;2, 1995.

https://doi.org/10.5194/egusphere-2026-4215
Preprint. Discussion started: 10 August 2026

Eyre, J. R., BROWNSCOMBE, J. L., and ALLAM, R. J.: Detection of fog at night using Advanced Very High Resolution Radiometer (AVHRR) imagery, Meteorol. Mag, 113, 266–271, 1984.

Gao, S., Lin, H., Shen, B., and Fu, G.: A heavy sea fog event over the Yellow Sea in March 2005: Analysis and numerical modeling, Adv. Atmos. Sci., 24, 65–81, https://doi.org/10.1007/s00376-007-0065-2, 2007.

Ghosh, P., Boutle, I., Field, P., Hill, A., Mazoyer, M., Evans, K. J., Mahajan, S., Kang, H.-G., Xu, M., Zhang, W., and Gordon, H.: Adiabatic and radiative cooling are both important causes of aerosol activation in simulated fog events in Europe, Atmospheric Chemistry and Physics, 25, 11157–11182, https://doi.org/10.5194/acp-25-11157-2025, 2025a.

Ghosh, P., Boutle, I., Field, P., Hill, A., Jones, A., Mazoyer, M., Evans, K. J., Mahajan, S., Kang, H.-G., Xu, M., Zhang, W., Asch, N., and Gordon, H.: High sensitivity of simulated fog properties to parameterized aerosol activation in case studies from ParisFog, Atmospheric Chemistry and Physics, 25, 11129–11156, https://doi.org/10.5194/acp-25-11129-2025, 2025b.

Gultepe I., Müller M. D., and Boybeyi Z.: A New Visibility Parameterization for Warm-Fog Applications in Numerical Weather Prediction Models, https://doi.org/10.1175/JAM2423.1, 2006.

Gultepe, I., Tardif, R., Michaelides, S. C., Cermak, J., Bott, A., Bendix, J., Müller, M. D., Pagowski, M., Hansen, B., Ellrod, G., Jacobs, W., Toth, G., and Cober, S. G.: Fog Research: A Review of Past Achievements and Future Perspectives, Pure appl. geophys., 164, 1121–1159, https://doi.org/10.1007/s00024-007-0211-x, 2007.

Hong, S.-Y., Noh, Y., and Dudhia, J.: A New Vertical Diffusion Package with an Explicit Treatment of Entrainment Processes, Monthly Weather Review, 134, 2318–2341, https://doi.org/10.1175/MWR3199.1, 2006.

Iacono, M. J., Mlawer, E. J., Clough, S. A., and Morcrette, J.: Impact of an improved longwave radiation model, RRTM, on the energy budget and thermodynamic properties of the NCAR community climate model, CCM3, J. Geophys. Res., 105, 14873–14890, https://doi.org/10.1029/2000JD900091, 2000.

Kain, J. S.: The Kain–Fritsch Convective Parameterization: An Update, Journal of Applied Meteorology and Climatology, 43, 170–181, https://doi.org/10.1175/1520-0450(2004)043%3C0170:TKCPAU%3E2.0.CO;2, 2004.

Kim, J., Kim, J., Dorman, C. E., and Fernando, H. J. S.: Numerical simulation and physical understanding of a locally initiated sea fog event over the eastern Yellow Sea with a

https://doi.org/10.5194/egusphere-2026-4215
Preprint. Discussion started: 10 August 2026

transition of air–sea temperature difference, Quart J Royal Meteoro Soc, e70228, https://doi.org/10.1002/qj.70228, 2026.

Kim, S., Moon, J.-H., and Kim, T.: A Coupled Numerical Modeling Study of a Sea Fog Case After the Passage of Typhoon Muifa Over the Yellow Sea in 2011, Journal of Geophysical Research: Atmospheres, 126, e2020JD033875, https://doi.org/10.1029/2020JD033875, 2021.

Köhler, H.: The nucleus in and the growth of hygroscopic droplets, Trans. Faraday Soc., 32, 1152–1161, https://doi.org/10.1039/TF9363201152, 1936.

Koračin, D. and Dorman, C. E. (Eds.): Marine Fog: Challenges and Advancements in Observations, Modeling, and Forecasting, Springer International Publishing, Cham, https://doi.org/10.1007/978-3-319-45229-6, 2017.

Koračin, D., Lewis, J., Thompson, W. T., Dorman, C. E., and Businger, J. A.: Transition of Stratus into Fog along the California Coast: Observations and Modeling, Journal of the Atmospheric Sciences, 58, 1714–1731, https://doi.org/10.1175/1520-0469(2001)058%3C1714:TOSIFA%3E2.0.CO;2, 2001.

Koračin, D., Dorman, C. E., Lewis, J. M., Hudson, J. G., Wilcox, E. M., and Torregrosa, A.: Marine fog: A review, Atmospheric Research, 143, 142–175, https://doi.org/10.1016/j.atmosres.2013.12.012, 2014.

Kunkel, B. A.: Parameterization of Droplet Terminal Velocity and Extinction Coefficient in Fog Models, Journal of Applied Meteorology and Climatology, 23, 34–41, https://doi.org/10.1175/1520-0450(1984)023%3C0034:PODTVA%3E2.0.CO;2, 1984.

Leipper, D. F.: Fog on the U.S. West Coast: A Review, 1994.

Lewis J. M., Koračin D., and Redmond K. T.: Sea Fog Research in the United Kingdom and United States: A Historical Essay Including Outlook, https://doi.org/10.1175/BAMS-85-3-395, 2004.

Li, S.-J., Liu, J.-W., and Ding, S.-S.: Effects of gravitational droplets sedimentation on the evolution of advection fog: Large-eddy simulations with interactive sectional microphysics, EGUsphere [preprint], https://doi.org/10.5194/egusphere-2026-2980, 2026.

Lin, Y.-L., Farley, R. D., and Orville, H. D.: Bulk Parameterization of the Snow Field in a Cloud Model, J. Climate Appl. Meteor., 22, 1065–1092, https://doi.org/10.1175/1520-0450(1983)022%3C1065:BPOTSF%3E2.0.CO;2, 1983.

https://doi.org/10.5194/egusphere-2026-4215
Preprint. Discussion started: 10 August 2026

Minnis, P., Yost, C. R., Sun-Mack, S., and Chen, Y.: Estimating the top altitude of optically thick ice clouds from thermal infrared satellite observations using CALIPSO data, Geophysical Research Letters, 35, https://doi.org/10.1029/2008GL033947, 2008.

Morrison, H., Thompson, G., and Tatarskii, V.: Impact of Cloud Microphysics on the Development of Trailing Stratiform Precipitation in a Simulated Squall Line: Comparison of One- and Two-Moment Schemes, https://doi.org/10.1175/2008MWR2556.1, 2009.

Nakanishi, M.: Large-Eddy Simulation Of Radiation Fog, Boundary-Layer Meteorology, 94, 461–493, https://doi.org/10.1023/A:1002490423389, 2000.

NASA/JPL: GHRSST Level 4 MUR Global Foundation Sea Surface Temperature Analysis (v4.1), https://doi.org/10.5067/GHGMR-4FJ04, 2015.

Peterka, A., Thompson, G., and Geresdi, I.: Numerical prediction of fog: A novel parameterization for droplet formation, Quarterly Journal of the Royal Meteorological Society, 150, 2203–2222, https://doi.org/10.1002/qj.4704, 2024.

Quinn, P. K., Coffman, D. J., Johnson, J. E., Upchurch, L. M., and Bates, T. S.: Small fraction of marine cloud condensation nuclei made up of sea spray aerosol, Nature Geosci, 10, 674–679, https://doi.org/10.1038/ngeo3003, 2017.

Remote Sensing Systems, Wentz, F., and Meissner, T.: RSS GCOM-W1 AMSR2 Daily Environmental Suite on 0.25 deg grid, Version 8.2, https://doi.org/10.56236/RSS-bq, 2024.

Rogers D. P. and Koračin D.: Radiative Transfer and Turbulence in the Cloud-topped Marine Atmospheric Boundary Layer, 1992.

Sasakawa, M. and Uematsu, M.: Chemical composition of aerosol, sea fog, and rainwater in the marine boundary layer of the northwestern North Pacific and its marginal seas, J.-Geophys.-Res., 107, https://doi.org/10.1029/2001JD001004, 2002.

Schwenkel, J. and Maronga, B.: Large-eddy simulation of radiation fog with comprehensive two-moment bulk microphysics: impact of different aerosol activation and condensation parameterizations, Atmos. Chem. Phys., 19, 7165–7181, https://doi.org/10.5194/acp-19-7165-2019, 2019.

Skamarock, C., Klemp, B., Dudhia, J., Gill, O., Liu, Z., Berner, J., Wang, W., Powers, G., Duda, G., Barker, D. M., and Huang, X.: A Description of the Advanced Research WRF Model Version 4, 2019.

Smith, A., Lott, N., and Vose, R.: The Integrated Surface Database: Recent Developments and Partnerships, Bulletin of the American Meteorological Society, 92, 704–708, https://doi.org/10.1175/2011BAMS3015.1, 2011.

https://doi.org/10.5194/egusphere-2026-4215
Preprint. Discussion started: 10 August 2026

Taylor, G. I.: The formation of fog and mist, Quarterly Journal of the Royal Meteorological Society, 43, 241–268, https://doi.org/10.1002/qj.49704318302, 1917.

Taylor, P. A., Chen, Z., Cheng, L., Afsharian, S., Weng, W., Isaac, G. A., Bullock, T. W., and Chen, Y.: Surface deposition of marine fog and its treatment in the Weather Research and Forecasting (WRF) model, Atmospheric Chemistry and Physics, 21, 14687–14702, https://doi.org/10.5194/acp-21-14687-2021, 2021.

Thompson, G. and Eidhammer, T.: A Study of Aerosol Impacts on Clouds and Precipitation Development in a Large Winter Cyclone, Journal of the Atmospheric Sciences, 71, 3636–3658, https://doi.org/10.1175/JAS-D-13-0305.1, 2014.

Tokinaga, H. and Xie, S.-P.: Ocean tidal cooling effect on summer sea fog over the Okhotsk Sea, Journal of Geophysical Research: Atmospheres, 114, https://doi.org/10.1029/2008JD011477, 2009.

Tokinaga, H., Tanimoto, Y., Xie, S.-P., Sampe, T., Tomita, H., and Ichikawa, H.: Ocean Frontal Effects on the Vertical Development of Clouds over the Western North Pacific: In Situ and Satellite Observations, Journal of Climate, 22, 4241–4260, https://doi.org/10.1175/2009JCLI2763.1, 2009.

Toledo, F., Haeffelin, M., Wærsted, E., and Dupont, J.-C.: A new conceptual model for adiabatic fog, Atmospheric Chemistry and Physics, 21, 13099–13117, https://doi.org/10.5194/acp-21-13099-2021, 2021.

Wærsted, E. G., Haeffelin, M., Dupont, J.-C., Delanoë, J., and Dubuisson, P.: Radiation in fog: quantification of the impact on fog liquid water based on ground-based remote sensing, Atmospheric Chemistry and Physics, 17, 10811–10835, https://doi.org/10.5194/acp-17-10811-2017, 2017.

Wang, binhua: Sea Fog, China Ocean Press, 1983.

Wang Y., Gao S., Fu G., Sun J., and Zhang S.: Assimilating MTSAT-Derived Humidity in Nowcasting Sea Fog over the Yellow Sea, https://doi.org/10.1175/WAF-D-12-00123.1, 2014.

Weston, M. J., Piketh, S. J., Burnet, F., Broccardo, S., Denjean, C., Bourrianne, T., and Formenti, P.: Sensitivity analysis of an aerosol-aware microphysics scheme in Weather Research and Forecasting (WRF) during case studies of fog in Namibia, Atmospheric Chemistry and Physics, 22, 10221–10245, https://doi.org/10.5194/acp-22-10221-2022, 2022.

Winker, D.: CALIPSO Lidar Level 1B profile data, V5-00, https://doi.org/10.5067/CALIOP/CALIPSO/CAL_LID_L1-STANDARD-V5-00, 2026.

https://doi.org/10.5194/egusphere-2026-4215
Preprint. Discussion started: 10 August 2026

Yamaguchi, T. and Randall, D. A.: Large-Eddy Simulation of Evaporatively Driven Entrainment in Cloud-Topped Mixed Layers, Journal of the Atmospheric Sciences, 65, 1481–1504, https://doi.org/10.1175/2007JAS2438.1, 2008.

Yang, L., Liu, J.-W., Ren, Z.-P., Xie, S.-P., Zhang, S.-P., and Gao, S.-H.: Atmospheric Conditions for Advection-Radiation Fog Over the Western Yellow Sea, Journal of Geophysical Research: Atmospheres, 123, 5455–5468, https://doi.org/10.1029/2017JD028088, 2018.

Yang, L., Liu, J.-W., Xie, S.-P., and Shen, S. S. P.: Transition from Fog to Stratus over the Northwest Pacific Ocean: Large-Eddy Simulation, Monthly Weather Review, 149, 2913–2925, https://doi.org/10.1175/MWR-D-20-0420.1, 2021.

Yang, L., Ding, S., Liu, J.-W., and Zhang, S.-P.: Effects of radiative cooling on advection fog over the northwest Pacific Ocean: observations and large-eddy simulations, Atmospheric Chemistry and Physics, 24, 6809–6824, https://doi.org/10.5194/acp-24-6809-2024, 2024.

Yang, Y. and Gao, S.: The Impact of Turbulent Diffusion Driven by Fog-Top Cooling on Sea Fog Development, Journal of Geophysical Research: Atmospheres, 125, e2019JD031562, https://doi.org/10.1029/2019JD031562, 2020.

Yang, Y., Hu, X.-M., Gao, S., and Wang, Y.: Sensitivity of WRF simulations with the YSU PBL scheme to the lowest model level height for a sea fog event over the Yellow Sea, Atmospheric Research, 215, 253–267, https://doi.org/10.1016/j.atmosres.2018.09.004, 2019.

Zhang, L., Shi, H., Gao, S., and Li, S.: Overestimated Fog-Top Entrainment in WRF Simulation Leading to Unrealistic Dissipation of Sea Fog: A Case Study, Remote Sensing, 16, 1656, https://doi.org/10.3390/rs16101656, 2024.

Zhang, S., Li, M., Meng, X., Fu, G., Ren, Z., and Gao, S.: A Comparison Study Between Spring and Summer Fogs in the Yellow Sea-Observations and Mechanisms, Pure Appl. Geophys., 169, 1001–1017, https://doi.org/10.1007/s00024-011-0358-3, 2012.